

Pressure-Driven Tearing and Thermal Transport in Finite-Beta Reversed Field Pinch Computations

U. Gupta and C. R. Sovinec

**University of Wisconsin-Madison
Center for Plasma Theory and Computation
Report UW-CPTC 22-4**

September 13, 2022

NOTICE

This report was prepared as an account of work sponsored by an agency of the United States Government. Neither the United States Government, nor any of its employees, makes any warranty, express or implied, or assumes any legal liability for the accuracy, completeness, or usefulness of any information, apparatus, product, or process disclosed, or represents that its use would not infringe privately owned rights. Reference herein to any specific commercial product, process, or service by trade name, trademark, manufacturer, or otherwise does not necessarily constitute or imply its endorsement, recommendation, or favoring by the United States Government or any agency thereof. The views and opinions of authors expressed herein do not necessarily state or reflect those of the United States Government or any agency thereof.

This research is supported by the U.S. Department of Energy (DOE) Grant No. DE-FG02-85ER53212. This research used resources of the National Energy Research Scientific Computing Center (NERSC), a U.S. Department of Energy Office of Science User Facility located at Lawrence Berkeley National Laboratory, operated under Contract No. DE-AC02-05CH11231 using NERSC award ERCAP0020418.

This article has been submitted to Physics of Plasmas for consideration for publication.

Pressure-driven tearing and thermal transport in finite-beta reversed field pinch computations

U. Gupta^{1,2} and C. R. Sovinec^{1,3}

¹*Center for Plasma Theory and Computation, 1500 Engineering Drive, Madison, Wisconsin 53706, USA*

²*Department of Physics, University of Wisconsin-Madison, 1150 University Avenue, Madison, Wisconsin 53706, USA*

³*Department of Engineering Physics, University of Wisconsin-Madison, 1500 University Avenue, Madison, Wisconsin 53706, USA*

(*Electronic mail: [Electronic mail: csovinec@wisc.edu](mailto:csovinec@wisc.edu))

(*Electronic mail: [Electronic mail: ugupta22@wisc.edu](mailto:ugupta22@wisc.edu))

(Dated: 4 September 2022)

Nonlinear resistive-MHD computation with heating and anisotropic transport is applied to examine the interaction between thermal energy and magnetic fluctuations in inductively driven reversed-field pinches (RFPs). The magnetic fluctuations underlie magnetic field reversal through dynamo-like correlations, and they enhance thermal energy transport through fluctuations of parallel heat-flux density. With the unfavorable magnetic curvature that exists across the RFP profile, thermal energy also affects the magnetic fluctuations. Computations with the NIMROD code [Sovinec, *et al.*, JCP **195**, 355 (2004)] integrate nonlinear MHD dynamics with energy transport and reproduce an RFP state with experimentally relevant values of plasma- β . Equilibria constructed from results of the 3D computations are analyzed to assess the sources of free energy in the saturated nonlinear state. Linear computations for these profiles show unstable modes of tearing parity. Their eigenfunctions are used to evaluate and compare stabilizing and destabilizing contributions to the kinetic energy integral. An assessment of the drives in the integral reveals that the pressure-gradient drive is of comparable magnitude to the parallel-current drive, and only the sum of the two surpasses the stabilizing contributions. Correlation of magnetic and parallel heat-flux-density fluctuations in the nonlinear computations shows that fluctuation-induced thermal conduction is the dominant mode of energy loss, as expected from experimental evidence. Decomposition of the fluctuating heat-flux density shows that second-order correlations, alone, do not explain the total energy transport. Higher-order correlations are also important.

I. INTRODUCTION

Research on the Reversed Field Pinch (RFP) magnetic confinement configuration has provided important insights on the science of plasma magnetic relaxation^[1] and fluctuation-induced transport^[2] while contributing to the development of a unique fusion energy concept.^[3,4] Relative to tokamaks and stellarators, the RFP has large engineering- β , which is defined as the ratio of plasma pressure and the magnetic pressure from the field that needs to be produced by external coils. The high β_E stems from the paramagnetic property of toroidal pinches, which is enhanced by the dy-

namo effect that leads to magnetic field reversal. With their large electrical current density, RFPs also offer the possibility of reaching burning-plasma conditions without an auxiliary heating system.^[4] Early observations of the characteristic reversal inspired Taylor's energy-minimization hypothesis. How relaxation occurs has been examined in detail through a combination of numerical computation^[5,12] and experiment.^[13,17] Large-scale magnetic tearing modes underlie the dynamics, and their tendency to produce stochastic magnetic topologies affects energy confinement.^[18,20] In this work, we apply nonlinear numerical simulation to study pressure-driven effects on magnetic tearing and the resulting transport. Although the modeling

of each aspect of the problem is necessarily simplified, the computations are relatively unique for magnetic confinement in self-consistently computing profile evolution, 3D nonlinear magnetohydrodynamics (MHD), heating, and transport.

Many nonlinear computations for RFPs focus on current-driven tearing dynamics, assuming that any pressure-driven effects are small. In fact, simulations taking the limit of vanishing plasma pressure reproduce the most notable RFP characteristics, such as field reversal, the tearing mode spectrum, and intermittency.^{[9][21][22]} This is understood from the fact that loop voltage in the presence of the highly sheared magnetic field in conventional RFPs produces a strong gradient in $\lambda = \mu_0 J_{\parallel} / B$, *i.e.* a strong current-gradient drive for MHD activity. In addition, magnetic stochasticity from tearing fluctuations leads to relatively flat profiles of plasma pressure in the core, where resonances are far from the stabilizing wall or feedback coils.

Nonetheless, plasma confinement requires a centrally peaked pressure profile. With the small safety-factor ($q < 1$), poloidal magnetic field dominates the average magnetic curvature and makes it unfavorable in conventional RFPs. Whereas the large magnetic shear suppresses ideal interchange,^[23] pressure can drive resistive interchange.^{[24][25]} It also affects the stability of tearing modes.^[26] A pressure gradient with unfavorable curvature alters the linear eigenfunction of the tearing mode near its resonant surface such that the sign of Δ' , where Δ' is the matching parameter, does not predict tearing-mode stability. When the Suydam parameter D is positive, Δ' can attain any value from $-\infty$ to $+\infty$, and no marginal stability criterion exists with an adiabatic closure for pressure.

This finding motivated several studies of linear resistive modes in RFP profiles. The analysis in Ref. [27] considers the importance of compressibility for Δ' -stable configurations and found a threshold in D for interchange stability. It is also shown that below a critical value of D , the growth rate of the tearing-parity mode for $\Delta' < 0$ scales like $(D/|\Delta'|)^4$, which can be very small. Computations in Ref. [28] demonstrate how pressure extends the spectrum of unstable modes with respect to axial wavenumber with a Suydam-marginal profile and finds that "resistive g-modes" always appear, although growth rates can be

vanishingly small at small- β . A later computational study found that crossing the Suydam threshold has very little effect on linear modes unless resistivity η is extremely small.^[29] It further examined the effects of varying the current profile when including a pressure gradient. Reference [30] considers the effects of varying D and η on the eigenfunctions of resonant $m = 1$ modes with small and large axial wavenumber (k) in $\Delta' < 0$ RFP profiles and finds that low- k modes maintain tearing structure when D is increased to the ideally unstable range. For the tearing mode, the radial component of displacement or flow-velocity is zero at the mode resonant surface and the radial component of the magnetic perturbation is non-zero; vice versa for interchange. Eigenfunctions have also been examined with an eigenvalue code that determines both tearing and interchange parities for each set of parameters, and the results for $\Delta' < 0$ profiles show that the transition for $m = 1$ occurs at β -values of 20-30%.^[31] That study also found that $m = 0$ modes maintain tearing parity to very large β -values.

The influence of thermal conduction is potentially important for the pressure-curvature drive for tearing modes. When considering how classical tearing in tokamaks transitions from linear to nonlinear behavior, Lütjens, Luciani, and Garbet found that thermal conduction can affect the outer-region solutions.^[32] If the scale for parallel thermal conduction to compete with perpendicular conduction in a magnetic-island^[33] is larger than the tearing layer, the dispersion relation has the form of the zero-pressure relation but with an altered value of Δ' . While this is a destabilizing effect in tokamaks, the analysis by Bruno, Freidberg, and Hastie shows that positive- D (pressure confining) conditions in RFPs can be stabilized by sufficiently negative values of Δ' .^[34] Mirza, Scheffel, and Johnson apply numerical computation to quantify the effect in $\Delta' < 0$ profiles and find that it reduces RFP growth rates for sufficiently small β and Lundquist numbers, $S \equiv \tau_r / \tau_A$, where τ_r is the resistive diffusion time, and τ_A is the Alfvén propagation time.^[35]

Nonlinear computations of MHD with pressure evolution have already contributed to our understanding of RFP dynamics. An early nonlinear study that restricted evolution to helical symmetry found that $m = 1$ resistive interchange saturates at

relatively small amplitude, but substantial $m = 0$ interchange results at large plasma- β .^[36] Some of the first 3D computational results on the dynamo effect includes Ohmic heating; however, the model has a sink of energy density throughout the domain to keep β small.^[6] Including anisotropic thermal conduction provides more realistic modeling of transport,^[37] which was then applied to examine the scaling of plasma- β with S .^[38] References [39] and [40] extend the scaling study to consider RFPs with current-profile control.^[8,41-44] Caveats on these earlier computations of energy transport are the fixed, uniform plasma density and the unphysically small aspect ratio R/a that was used to reduce computational costs by limiting the magnetic fluctuation spectrum. More recent studies include density evolution at realistic aspect ratio and demonstrate the evolution of temperature to a centrally flat profile when including rapid parallel thermal conduction.^[45,46]

Nonlinear simulations of RFP relaxation with a low-frequency two-fluid model^[11,12] also consider pressure evolution. Nonzero plasma pressure is needed to produce important finite-Larmor-radius effects on tearing.^[47,48] However, the background pressure in the computations is uniform to focus on core current-gradient driven dynamics without the computational challenges of having the pressure-gradient drive.

The aim of the present study is to determine the role of pressure in sustaining tearing fluctuations in relaxed RFP states.^[49] We also examine the fluctuation-induced transport processes that are represented in a self-consistent resistive-MHD model with anisotropic thermal conduction and heating. The remainder of this paper is organized as follows: In Section [I] we describe our physical parameters and numerical methods. Particular attention is devoted to the symmetric steady-state fields used in our simulations. Section [II] describes the transient phase of our time-dependent computations, which produces relaxed configurations from the initial symmetric states. Section [IV] presents analysis of the simulated sustained RFP conditions. Linear computations of equilibria constructed from the relaxed 3D nonlinear results are applied to analyze the driving sources of free energy. We also examine the energy and particle transport that is represented by

the nonlinear MHD computations. Finally in Section [V] we summarize and draw conclusions from our study.

II. METHODS AND PARAMETERS

A. Numerical Methods and Boundary Conditions

The 3D nonlinear computations presented in this paper have been performed using the initial value Non-Ideal Magnetohydrodynamics with Rotation, Open Discussion (NIMROD) code.^[50] NIMROD applies spectral finite elements in a two-dimensional plane and Fourier series representation in the third, periodic direction. The temporal evolution is a semi-implicit advance which allows time stepping (Δt) independent of Alfvénic propagation. We restrict the time steps to a flow-based Courant Freidrichs Lewy (CFL) condition for numerical accuracy.

Our computations have been performed in cylindrical geometry with a circular cross-section of radius $a = 1.0$ and periodic length $L = 2\pi R$, where $R = 3$ is the major radius of the analogous torus. We have used the spectral finite element representation over the two dimensional poloidal plane and finite Fourier series representation in the axial direction of the cylinder. The poloidal plane has a 32×32 (radial \times azimuthal) annular mesh of biquartic rectangular elements surrounding a central region of 192 biquartic elements. This mesh departs from a strictly polar mesh in which thin elements meet at a central point; using the non-polar mesh moderates the CFL number for a given Δt . The axial direction is represented by 86 Fourier harmonics denoted by n ranging from 0 to 85. The poloidal harmonics are only restricted by the mesh scale and are denoted by m . Homogeneous Dirichlet boundary conditions are applied to $\hat{\mathbf{n}} \cdot \mathbf{B}$ at $r = 1$, representing a conducting shell, and no-slip conditions are applied on the flow. Homogeneous Dirichlet conditions are also applied to temperature and density perturbations, so that the physical fields are prescribed by the input steady fields that are describe in Section [II C].

NIMEQ^[51] is a general purpose Grad Shafranov solver developed for NIMROD's spectral-element representation. We use it to construct high-quality

equilibria for profiles extracted from nonlinear NIMROD calculations. These equilibria provide the basis for analyzing free energy in the NIMROD-computed relaxed states. We apply field-line tracing to the $n = 0$ part of the nonlinear NIMROD computations to obtain the flux-averaged profiles of pressure $P(\psi)$ and $F(\psi) = RB_z$. With these profiles, NIMEQ is used to solve the GS equation:^{[52][53]}

$$\Delta^* \psi = -\mu_0 R^2 P'(\psi) - FF'(\psi)$$

where the GS operator is

$$\Delta^* \equiv R \frac{\partial}{\partial R} R^{-1} \frac{\partial}{\partial R} + \frac{\partial^2}{\partial Z^2}$$

and primes indicate differentiation with respect to ψ .

The field-line tracing diagnostic also enables us to obtain and analyze profiles of flux-averaged quantities such as the safety-factor, parallel current, density and temperature at different times during our non-linear computations.

B. Physical parameters

We first define the relevant physical quantities. The magnetic field and electric field are represented by \mathbf{B} and \mathbf{E} , respectively. The current density is denoted by \mathbf{J} . The symbols p , n and T are the total pressure, species particle density and temperature of the plasma and subscripts "i" and "e" are used to indicate ion and electron species, respectively. The center of mass flow velocity is denoted by \mathbf{V} . All physical constants such as the vacuum magnetic permeability μ_0 , the Boltzmann constant k_B , mass of ions m_i and charge of ions q_i have been normalized to 1.0 in our computations. The magnitude of plasma parameters that characterize the computations presented here are chosen so as to represent the single fluid plasma-MHD regime while also being computationally tractable. The resulting relaxed states have Alfvén speed $v_A = B/\sqrt{\mu_0 m_i n} \sim 1$, so the Lundquist number $S = \mu_0/\eta$, where η/μ_0 is the resistive diffusivity, and we set $S = 40000$. The magnetic Prandtl number is $\text{Pm} = \mu_0 \nu/\eta$, where ν is the isotropic viscosity. It is set to 5 over the final

phase of our simulations, where we analyze free energy and transport. Our S -value is approximately 100 times smaller than what is achieved in large RFP experiments, and smaller- S reduces intermittency (RFP sawtooth) in the MHD dynamics.^[9]

C. Equilibrium Configuration

NIMROD has been implemented to evolve nonlinear perturbations about a prescribed symmetric steady state without assuming an ordering on the size of the perturbations. It is also used for time-dependent linear computations, where all nonlinear terms are excluded. While any 2D MHD equilibrium may be used, nonlinear time-dependent computations with profiles that do not satisfy the steady-state limit of the dynamical equations effectively contain implicit sources. Because our aim is to investigate pressure-driven dynamics and global energy transport self-consistently with magnetic relaxation, we use profiles that satisfy steady-state relations for magnetic field, particle density, and temperature. For a given value of applied voltage and given profiles of electrical resistivity and thermal conductivity, the unique cylindrical 1D steady state in cylindrical geometry is a "stabilized" z -pinch without a radial pinch flow, $\mathbf{V} = \mathbf{E} \times \mathbf{B}/B^2 = 0$. The axial guide field B_z and the axial electric field $E_z = \eta(r)J_z$ are uniform. E_z is then curl-free and implies a uniform loop voltage for sustaining the plasma current. For cylindrical geometry, the following set of 1D ODEs is solved numerically to obtain a desired steady state:

$$\frac{dp}{dr} = -B_\theta \frac{E_z}{\eta(r)} \quad (1)$$

$$\frac{d}{dr}(rB_\theta) = \mu_0 r \frac{E_z}{\eta(r)} \quad (2)$$

$$\frac{d\Theta_\perp}{dr} = -(\Gamma - 1) f_e \frac{rE_z^2}{\eta(r)} \quad (3)$$

$$\frac{dn}{dr} = -\frac{n}{p} \left[\frac{B_\theta E_z}{\eta(r)} + \frac{\Theta_\perp}{r f_e \chi_\perp} \right] \quad (4)$$

where

$$\Theta_\perp = rn(r)\chi_\perp(r) \frac{dT}{dr}. \quad (5)$$

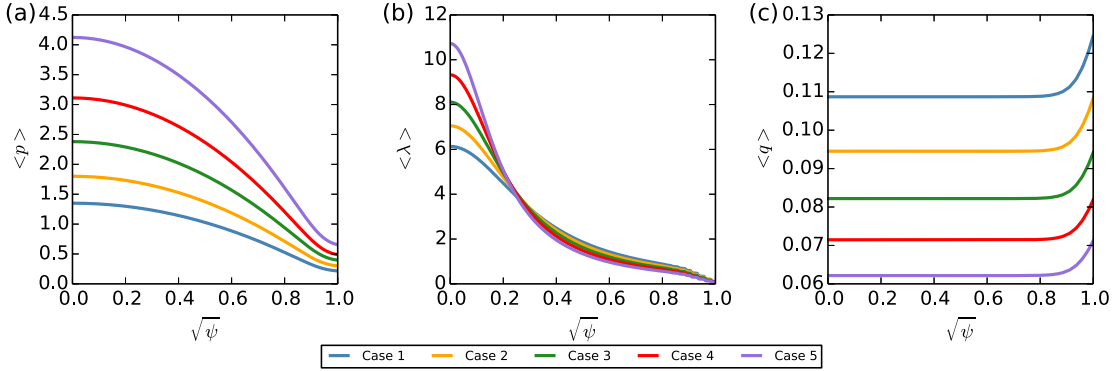


FIG. 1: Flux surface average profiles (a) Pressure, (b) Parallel Current, (c) Safety Factor for different steady states.

Eq. [1] is the steady-state force balance, and Eq. [2] is Ampere's law, where current density in each is taken from Ohm's law. Eq. [3] describes steady-state thermal transport with balanced perpendicular thermal conduction and Ohmic heating. The perpendicular thermal diffusivity χ_{\perp} is uniform, and $\Gamma = 5/3$ is the adiabatic index for an ideal monatomic gas. Quasi-neutrality is assumed ($n_e \approx n_i \approx n$). To find a relation for the density gradient (Eq. [4]), the temperature is substituted into Eq. [5] using the ideal gas relation ($p_e = f_e p = n T_e$). In this work, ion and electron temperatures are equal ($f_e = 0.5$), which models rapid thermal equilibration.

Five different steady states have been computed by varying the E_z drive. The computations have been named Cases 1-5 in increasing order of the drive. For each of these five cases, the resistivity is uniform with $\eta_0 = 2.5 \times 10^{-5}$ in the core and peaks in a narrow region near the wall $\eta(r) = \eta_0 [1 + (\sqrt{10} - 1)r^{24}]^2$ to approximate low temperature at the edge. They also have axial field of $B_z = 0.375$ to produce $B \sim 1$ after relaxation. The steady states are then uniquely determined by their axial current density profiles $J_z(r) = E_z/\eta(r)$. Each case has uniform core current density J_z over $r < 0.9a$ with values between 2.0 and 5.0 for the different steady states. The equilibria have strong gradients in the parallel current profiles $\lambda(r) = a\mu_0 \mathbf{J} \cdot \mathbf{B}/B^2$, as shown in Figure [1](b). Each steady state also has a pressure-curvature drive (Figure [1](a)). The safety-factor profiles $q(r) = rB_z(r)/RB_{\theta}(r)$ (Figure [1](c)) are

uniform in the core, indicating the absence of magnetic shear

The axial component of the pinch fields used as NIMROD's symmetric steady fields reduces the growth rates of ideal-MHD kink and sausage modes. However, the profiles are still violently unstable to kink, sausage, and other interchange modes. The initial phase of our time-dependent computations, described in Section [III], relaxes these unstable profiles. The main finding there is that the simulations succeed in achieving representative relaxed states. Our experience with an alternative approach of using vacuum magnetic field and uniform particle density for the steady-state fields, and applying voltage through a boundary condition for the $n = 0$ part of the evolving solution, is that strong pinching of the particle density prevents progression to a relaxed state.

D. Time-dependent Computations

The nonlinear evolution of particle density, momentum density, and temperature from the prescribed steady states are modeled by the following

equations:

$$\frac{dn}{dt} + n\nabla \cdot \mathbf{V} = \nabla \cdot D\nabla n \quad (6)$$

$$mn \frac{d\mathbf{V}}{dt} = \mathbf{J} \times \mathbf{B} - \nabla p + \nu \nabla \cdot (mn \mathbf{W}) - m \mathbf{V} \nabla \cdot (D\nabla n) \quad (7)$$

$$\frac{n}{\Gamma - 1} \frac{dT}{dt} = -\frac{p}{2} \nabla \cdot \mathbf{V} - \nabla \cdot \mathbf{q} + \eta \mathbf{J}^2 + \nu \rho \nabla \nabla^T : \nabla \mathbf{V} + \left(\frac{f_{im} V^2}{2} - \frac{T}{Z_{eff}(\Gamma - 1)} \right) \nabla \cdot D\nabla n \quad (8)$$

where

$$\mathbf{q} = -n[\hat{\mathbf{b}}\hat{\mathbf{b}}\chi_{\parallel} + (\mathbf{I} - \hat{\mathbf{b}}\hat{\mathbf{b}})\chi_{\perp}] \cdot \nabla T. \quad (9)$$

For clarity, the steady-state fields are not shown explicitly but are shown in Eq. 4 of Ref. [50]. The electron momentum equation is represented by neglecting two-fluid contributions and inertial terms, leading to the resistive MHD Ohm's law:

$$\mathbf{E} = -\mathbf{V} \times \mathbf{B} + \eta \mathbf{J}. \quad (10)$$

In addition to the above, our model uses Faraday's law, $\partial \mathbf{B} / \partial t = -\nabla \times \mathbf{E}$ and Ampere's law without displacement current, $\mu_0 \mathbf{J} = \nabla \times \mathbf{B}$, for low-frequency dynamics. The continuity equation (Eq. 6) includes a particle diffusion term that is used for the purpose of numerical smoothing at the node scale, and we set $D = 1.0 \times 10^{-5}$. This also requires additional numerical force density and heat density terms, the last terms in Eq. 7-Eq. 8, for conservation of momentum and energy. [See the appendix of Ref. [54] In Eq. 7, $\mathbf{W} = \nabla \mathbf{V} + \nabla \mathbf{V}^T - (2/3)\mathbf{I}\nabla \cdot \mathbf{V}$ is the rate of strain tensor. Eq. 8 describes thermal transport with anisotropic thermal conduction (\mathbf{q}) and Ohmic heating ($\eta \mathbf{J}^2$). Thermal diffusivities χ_{\parallel} and χ_{\perp} are uniform with $\chi_{\perp} = 2.5 \times 10^{-5}$ and $\chi_{\parallel} / \chi_{\perp} = 4 \times 10^4$. The last term is the viscous heating source ($\nu \rho \nabla \nabla^T : \nabla \mathbf{V}$) that is switched on and off in the computations to assess its impact on the computations.

III. INITIAL EVOLUTION

With the exception of the numerical particle diffusion terms, the computed steady states described in Section II C satisfy the time-independent form of our evolution equations, Eqs. 6-8 and Faraday's law. NIMROD's evolution of perturbations from these states is then consistent for the physical parameters, plus an effective particle source density that counteracts diffusion of the steady density profile. Asymmetric perturbations for our time-dependent computations are initialized at small amplitude. The low-shear steady states are violently unstable to ideal-MHD interchange. We facilitate computations through this transient phase by setting the isotropic viscosity to make $\text{Pm} = 500$, which allows the simulations to progress toward lower-energy RFP profiles. Section III A describes in the evolution of energy spectra from the highest-current steady state that is qualitatively representative of all the five and produces a final state that is closest to achieving reversal. In Section III B we modify the steady-state fields to achieve conditions with a realistic value of β and sustained field reversal.

A. Development of High- β Profiles

Nonlinear saturation of the ideally unstable perturbations causes the profiles to undergo a strong relaxation event in the first 40-100 Alfvén times. During this phase, both the pressure and parallel current undergo substantial flattening in the core, which develops magnetic shear, as shown by the traces of the safety factor profile in Figure 2. The sausage instability with $(m, n) = (0, 1)$ is the dominant fluctuation at this time, but other $n < 15$ perturbations also have large energy (Figure 3). Among the $m > 0$ perturbations, those with $n < 10$ are $m = 1$, whereas $n > 10$ perturbations are primarily $m \geq 2$. We infer from the strong pressure gradients of these equilibria that the high poloidal mode numbers have an ideal MHD interchange character. The radial component of magnetic field for some of these fluctuations (Figure 4 shows $n = 14$) is observed to have an odd- B_r , *i.e.* interchange, parity. At around $t = 250 \tau_A$, the perturbations begin settling into a partially stabilized saturated state, while the remaining edge gradients

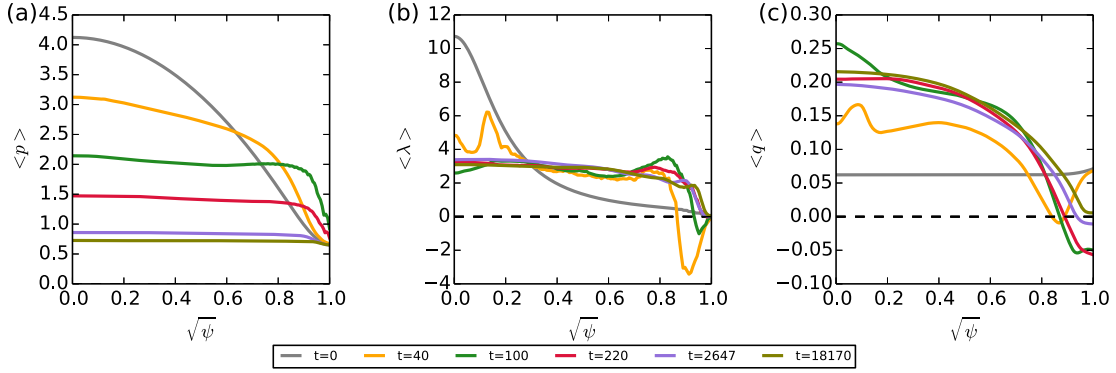


FIG. 2: Temporal Variation in flux averaged (a) Pressure, (b) Parallel Current, and (c) Safety-factor during non-linear evolution of profiles in Case 5.

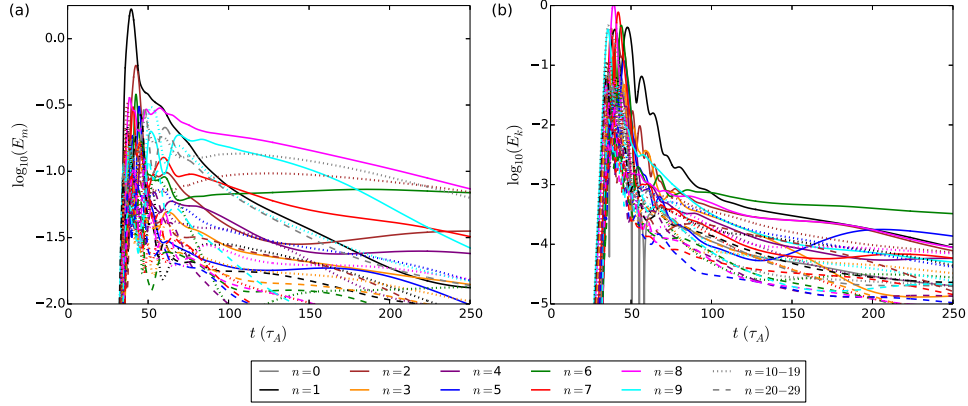


FIG. 3: Temporal evolution of spectral energies (a) Magnetic Energy, (b) Kinetic Energy for Case 5 at $Pm=500$ for $t < 250 \tau_A$. The color sequence is repeated for $n \geq 10$ with the patterns indicated in the figure legend.

of pressure and parallel current continue to undergo further relaxation.

Once a quasi-steady state is reached, we lower Pm to 20 by decreasing the viscous dissipation and allowing the perturbations to evolve further. Another small relaxation event occurs, which is indicated by the spike in the spectra at $t=2500 \tau_A$ (Figure 5), followed by further flattening of edge gradients until a saturated state is reached. The late-time quasi-steady state has a safety factor profile with a value on axis close to 0.2 as observed for

$t=18170 \tau_A$ in Figure 2(c). As expected from the q -profile, the $m=1$, $5 \leq n \leq 8$ fluctuations then dominate the fluctuation spectrum. Thus, a final state that approaches the RFP has been computationally obtained, starting from the unstable cylindrical pinch.

Similar features of nonlinear evolution are produced in all of the Cases 1-5. The final pressure, safety factor, and parallel current profiles are compared for these different computations in Figure 6. With increasing current drive, the safety-factor profile shifts closer to an RFP state. The obtained final

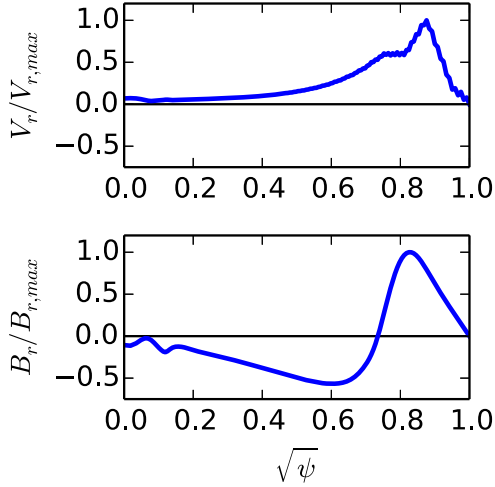


FIG. 4: Radial components of \mathbf{V} and \mathbf{B} from the linear eigenfunction of the $n=14$ axial mode obtained from an equilibrium extracted at $t=50 \tau_A$ during initial evolution.

pressure profiles are flat throughout the core. The pressure at the edge of the domain is a significant fraction of the central pressure and does not tend to zero, due to the boundary conditions on temperature and density, which maintain the values of the initial pinch states. In addition, $\beta > 1$ in these results, and compressibility is an important factor for the persistence of reversal in RFPs. Previous computations have found that high pressure or an incompressibility constraint leads to loss of reversal after an initial relaxation event.^{[55][56]} Here, reversal in the q -profile is observed briefly during the initial transient phase but is not sustained, even with the highest current drive.

B. Experimentally Relevant β -Values

The computations described above produce unrealistic final states with $\beta > 1$, and they do not sustain toroidal field reversal. To replicate RFP-relevant conditions, we replace the Case 5 steady-state profile with one computed using the method

described in Section III C for a spatially uniform η -profile. With smaller resistivity near the edge, the equilibrium has larger perpendicular current density in that region, which supports a pressure gradient such that the pressure approaches zero near the wall. To avoid the violent initial transient, the perturbations from Case 5 at $t=8725 \tau_A$ are used as the initial conditions for the new steady state. The magnetic Prandtl number is reduced to 5 by further lowering the viscosity, and the nonlinear perturbations are allowed to evolve until saturation. The evolution of the pressure profile to a low- β saturated state is shown in Figure 7(b). Thermal transport with the small edge pressure results in a realistic $\beta \sim 0.1$ at saturation. The parallel current profile is very similar to the profile in the high- β final state.

With the increased compressibility at lower pressure, the low- β computations produce significant toroidal field reversal during relaxation. The reversal parameter $F = \pi a^2 \langle B_z(a) \rangle / \Phi_z$, where Φ_z is the axial magnetic flux and $\langle \rangle$ indicates a surface average, settles to a value of ~ -0.040 , and the pinch parameter $\Theta = \pi a^2 \langle B_\theta(a) \rangle / \Phi_z$ at saturation is ~ 1.79 . These values are close to those obtained in reversed MST experiments.^{[57][58]}

As shown in Figure 8, the dominant perturbations at saturation are in the range $5 \leq n \leq 8$ with $n=5$ and $n=7$ competing for the highest energies. The $n=6$ mode may also be dominant intermittently during the evolution. As discussed later, the parity of the modes confirms their tearing character. The $(m,n)=(2,10)$ mode, which is a harmonic of the $(1,5)$ mode, is also large at times.

The sustainment of field reversal results from the non-linear dynamo effect that transfers energy from the poloidal magnetic field to the toroidal magnetic field.^[59] Both the MHD dynamo and the Hall dynamo contribute significantly to this phenomenon.^{[11][21][64][60][62]} The simulations presented here are single-fluid MHD computations, so the Hall dynamo is not represented. Figure 9 shows time-averaged components of the MHD dynamo power density in the $\text{Pm}=5$ saturated state. The $4\pi^2 R r$ factor represents the cylindrical surface area to show net power per unit radius, and the sign indicates the direction of flow with a positive value implying transfer of energy from the mean field to the fluctuations. The dominant fluctuations $5 \leq n \leq 9$

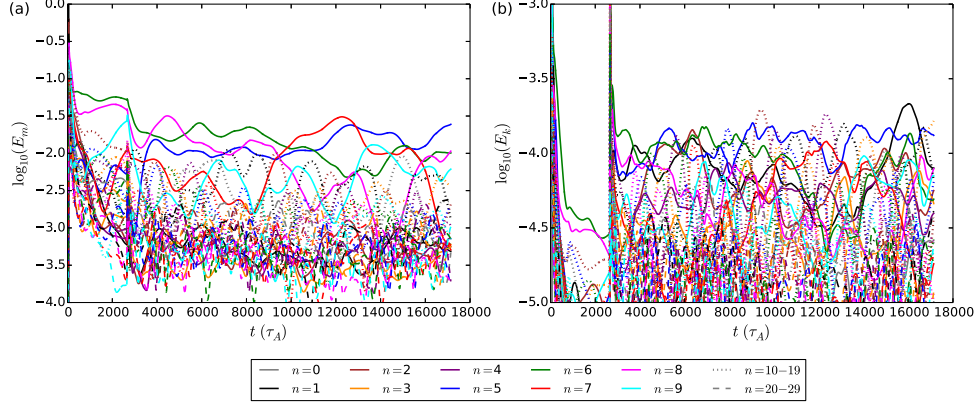


FIG. 5: Temporal evolution of spectral energies (a) Magnetic Energy (b) Kinetic energy for Case 5 with $Pm=20$ for $t > 250 \tau_A$.

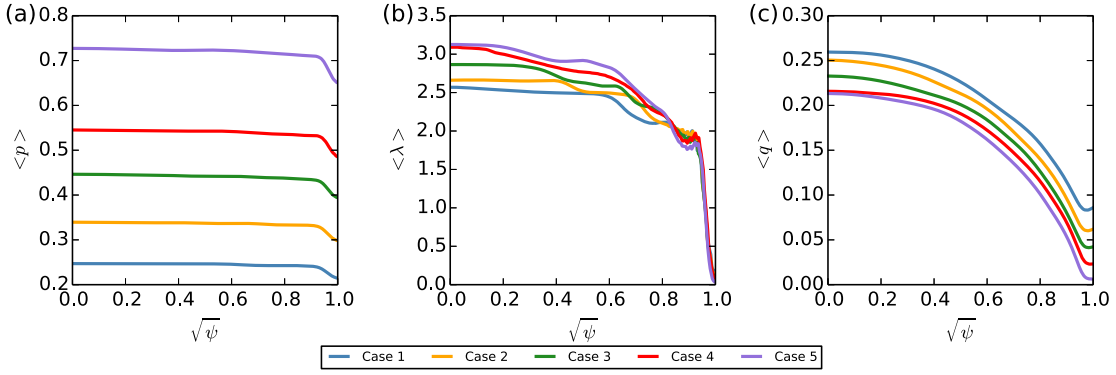


FIG. 6: Flux surface average of (a) Pressure, (b) Parallel Current, and (c) Safety Factor in the final states of the non-linear computations for Cases 1-5.

extract significant power from the axial component of plasma current density. A comparable amount of power is deposited into the poloidal component of current density via the same set of tearing modes. This drive of poloidal current density sustains the reversed field in the presence of resistive diffusion.

We have also performed the low- β computation with viscous heating. The non-linear evolution is similar to that described above, which is expected from the relatively small kinetic energy density. For the computation with viscous heating, the reversal parameter in the final state is ~ -0.043 and the

pinch parameter is ~ 1.80 .

IV. PLASMA PRESSURE AND TRANSPORT

Here, we assess the effects of the pressure-curvature drive in the computed RFP states and study the energy transport that occurs in the RFP model.

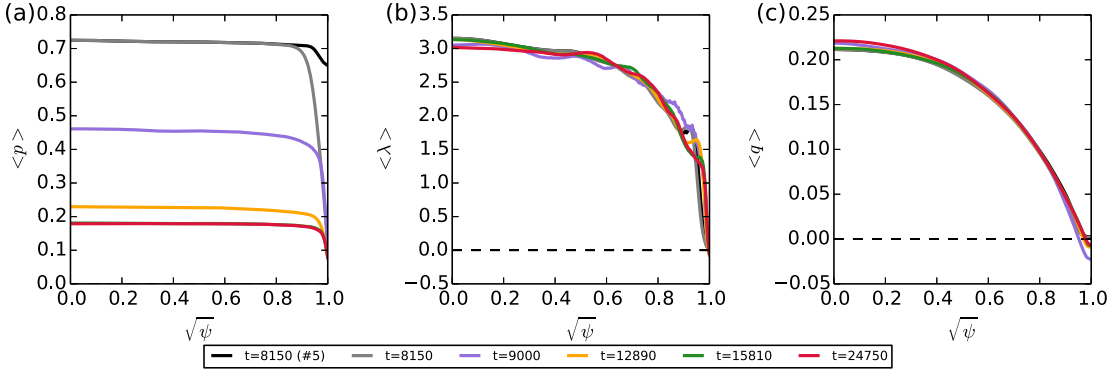


FIG. 7: Temporal evolution of profiles of flux averaged quantities - (a) Pressure, (b) Parallel Current and (c) Safety Factor for the low- β computation.

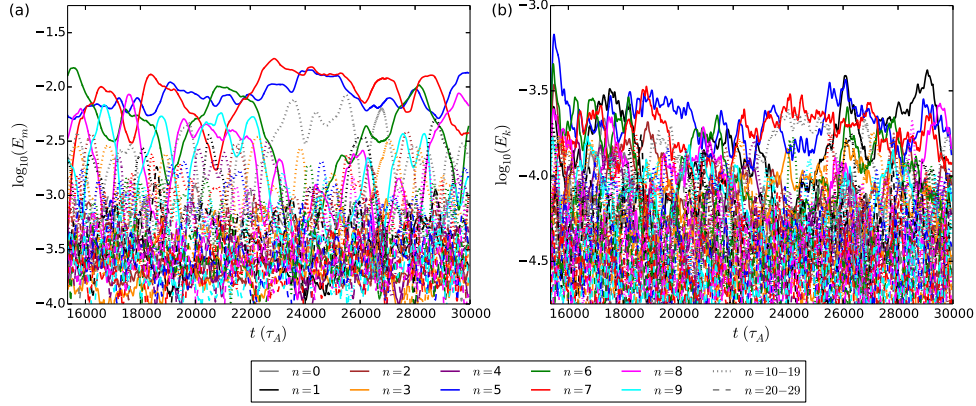


FIG. 8: Temporal evolution of spectral energies (a) Magnetic Energy, (b) Kinetic Energy for the low- β computation at $\text{Pm}=5$.

A. Assessment of the Pressure Drive

We characterize the role of pressure in driving the tearing modes in the relaxed low- β RFP through linear analysis. We use the method described in Section II to obtain $P(\psi)$ and $F(\psi)$ profiles at specific intervals from the two low- β 3D nonlinear computations that are identical except for viscous heating. We then find temporally averaged pressure and current functions from different times in each nonlinear computation. NIMEQ is used to solve the

GS equation with the time-averaged profiles to obtain equilibria for linear analysis.

The linear computations described here have been performed with the single-fluid resistive-MHD model used for the nonlinear computations. The Lundquist number $S=40000$ is the same as that of the nonlinear computations. Viscosity is reduced in the core such that $\text{Pm}=0.001$ to minimize dissipative effect on the tearing mode. However, high viscosity is retained in the edge to suppress $m=0$ Suydam modes that are resonant near the large edge pressure gradient. To further simplify the following analy-

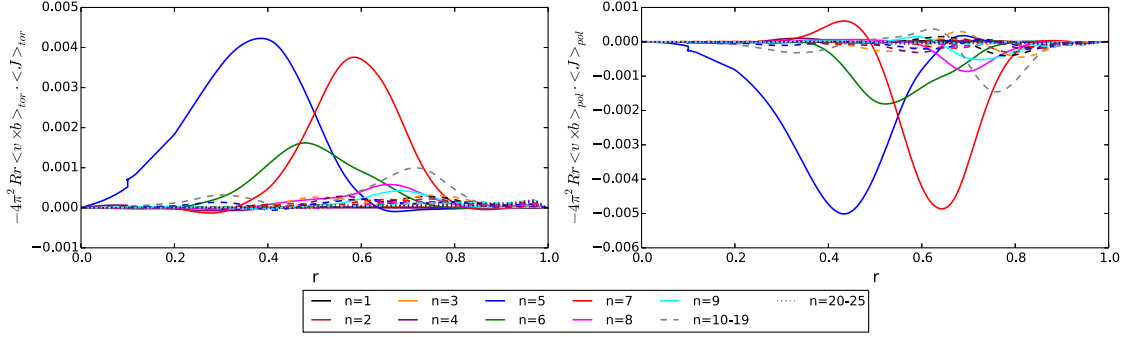


FIG. 9: Time-averaged MHD Power transfer for $Pm=5$ saturated state of the low- β computation. The small kink in the $n = 5$ trace is an artifact of the non-annular mesh near $r = 0$.

sis, only a very small amount of isotropic thermal diffusivity ($\mu_0\chi/\eta = 0.001$) is used so that the system is nearly adiabatic. High spatial resolution and mesh packing near the tearing mode resonant surfaces has been used to ensure that the eigenmodes are well resolved. The computations find $n=6-9$ to be unstable, and their eigenfunctions are analyzed here. Although it has significant amplitude in the nonlinear simulations, computations with the time-averaged profiles indicate that $n = 5$ is linearly stable. Plots of the radial component of the magnetic field and the radial component of the velocity for the unstable eigenmodes as a function of the flux coordinate $\sqrt{\psi}$ are shown in Figure 10. V_r for each mode passes through zero, and $B_r(r_s)$ is non-zero, at the rational surface for each mode. Each of these modes is thus confirmed to have a tearing parity.

The perturbed kinetic energy from linear calculations can be analyzed to compare the drive terms and develop insights about tearing instabilities in RFP equilibria. The kinetic energy integral is obtained by taking the dot product of the flow vector (\mathbf{V}) with the momentum equation. For equilibria with no background flow i.e. $\mathbf{V}_0 = 0$, we can use $\frac{\partial}{\partial t} \rightarrow \gamma$ (where γ is the linear growth rate of the respective eigenmode) to describe time dependence. We therefore have:

$$-\gamma^2 \int dVol \left[mn_0 \frac{|V_n|^2}{2} \right] = \int dVol \left[-\mathbf{V}_n \cdot (\mathbf{J}_0 \times \gamma \mathbf{B}_n) - \mathbf{V}_n \cdot \left[(\nabla \times \frac{\gamma}{\mu_0} \mathbf{B}_n \times \mathbf{B}_0) + \mathbf{V}_n \cdot \nabla \gamma P_n \right] \right] \quad (11)$$

The subscript 0 refers to equilibrium fields. Hereafter, the subscript n referring to a specific linear mode is suppressed for brevity.

In the same spirit, Faraday's law can be expressed as follows:

$$\frac{\partial \mathbf{B}}{\partial t} = \gamma \mathbf{B} = \nabla \times (\mathbf{V} \times \mathbf{B}_0 - \eta \mathbf{J}) \quad (12)$$

In the above equation, $\mathbf{E} = -\mathbf{V} \times \mathbf{B}_0 + \eta \mathbf{J}$ is the resistive MHD Ohm's law. We define the first term on the RHS as $\mathbf{Q}_i = \nabla \times (\mathbf{V} \times \mathbf{B}_0)$ representing the ideal part of Ohm's law. The second term is the contribution from resistive diffusion with uniform η :

$$Q_\eta = -\eta \nabla \times \mathbf{J} = \eta \nabla^2 \mathbf{B} \quad (13)$$

Similarly, the evolution of perturbed pressure can be expanded in terms of the background pressure gradient using the adiabatic closure:

$$\frac{\partial P}{\partial t} = \gamma P = -\mathbf{V} \cdot \nabla P_0 - \Gamma P_0 \nabla \cdot \mathbf{V} \quad (14)$$

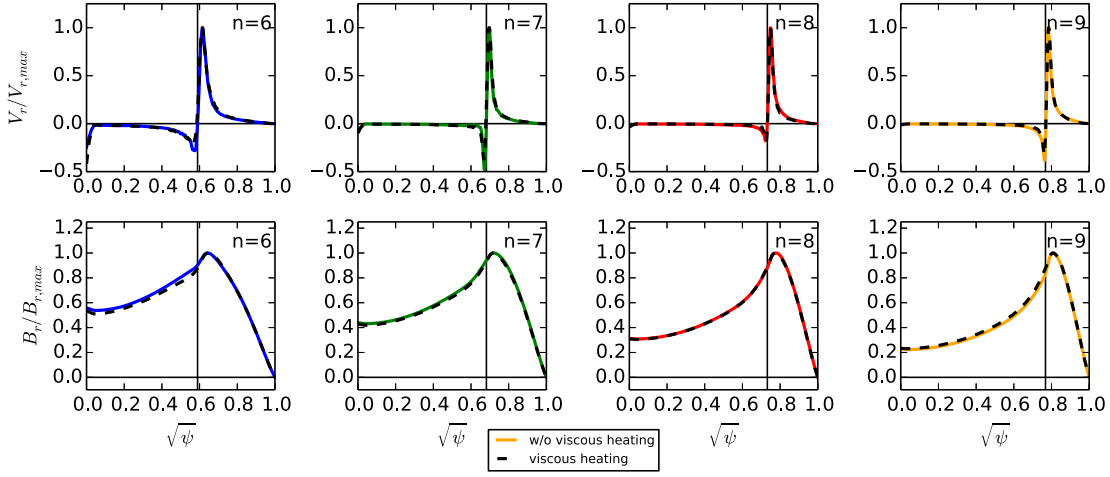


FIG. 10: Eigenfunction components V_r and B_r of $n = 6-9$ as a function of the flux coordinate. That $V_r = 0$ and $B_r \neq 0$ at the resonant surface of the corresponding mode indicates that each has tearing parity.

Substituting the relations for $\gamma\mathbf{B}$ and γP into the volume integral of kinetic energy, we obtain:

$$-\gamma^2 \int dVol \left\{ mn_0 \frac{|V|^2}{2} \right\} = \int dVol \left[-\mathbf{V} \cdot [\mathbf{J}_0 \times (\mathbf{Q}_i + \mathbf{Q}_\eta)] - \mathbf{V} \cdot [(\nabla \times (\mathbf{Q}_i + \mathbf{Q}_\eta)) \times \mathbf{B}_0] + \mathbf{V} \cdot \nabla [\mathbf{V} \cdot \nabla P_0 + \Gamma P_0 \nabla \cdot \mathbf{V}] \right] \quad (15)$$

Applying vector calculus identities and conducting wall boundary conditions ($V_r(a) = B_r(a) = 0$) to any surface terms, and identifying magnetic curvature $\kappa = \hat{\mathbf{b}}_0 \cdot \hat{\mathbf{b}}_0$, the above equation can be expressed as:

$$-\gamma^2 \int dVol \left\{ mn_0 \frac{|V|^2}{2} \right\} = \int dVol \left[|\mathbf{Q}_\perp|^2 + B_0^2 |\nabla \cdot \mathbf{V} + 2\mathbf{V} \cdot \kappa| + \Gamma P_0 |\nabla \cdot \mathbf{V}|^2 - \lambda \mathbf{Q}_i \cdot (\mathbf{V}_\perp \times \mathbf{B}_0) - 2(\mathbf{V}_\perp \cdot \nabla P_0)(\mathbf{V} \cdot \kappa) + \mathbf{Q}_\eta \cdot \mathbf{Q}_i - \lambda \mathbf{Q}_\eta \cdot (\mathbf{V}_\perp \times \mathbf{B}_0) - \frac{1}{B_0^2} (\mathbf{Q}_\eta \cdot \mathbf{B}_0)(\mathbf{V}_\perp \cdot \nabla P_0) + \frac{1}{B_0^2} (\mathbf{Q}_\eta \cdot \nabla P_0)(\mathbf{V}_\perp \cdot \mathbf{B}_0) \right] \quad (16)$$

The first three terms of this kinetic-energy relation are positive-definite and resemble the stabilizing contributions of field-line bending energy, magnetoacoustic wave, and compressional waves of the intuitive form of the well known ideal-MHD energy principle⁶³. Similarly, the next two terms are the parallel current drive and pressure drive. The

last four terms containing \mathbf{Q}_η represent resistive analogs of the ideal-MHD terms. A diagnostic has been developed to evaluate each of these terms for eigenfunctions of linear computations. Their relative magnitudes are assessed to understand the significance of the pressure drive in the tearing activity in our nonlinear RFP simulations.

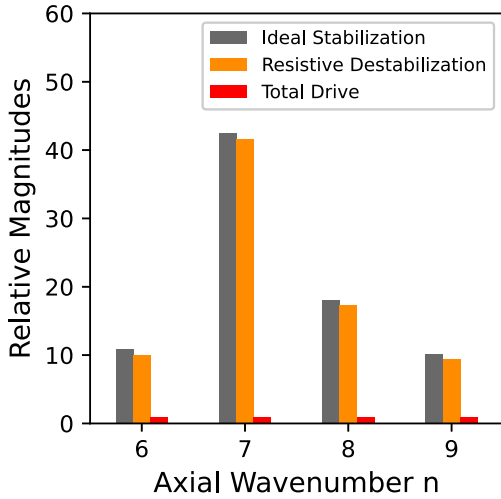


FIG. 11: Kinetic energy integral terms, grouped by ideal and resistive contributions and compared with the total drive for each eigenmode. The analyzed eigenmodes are for the time-averaged profiles from the nonlinear low- β computation without viscous heating. Magnitudes are normalized by the total drive for each mode.

In Figure 11, we evaluate and compare the magnitude of contributions to the kinetic energy integral from the total ideal stabilizing terms, the total resistive terms, and the total drive terms for each linear eigenmode from $n = 6$ to $n = 9$. The signs of the terms have been suppressed to compare magnitudes only, and each term is henceforth described as stabilizing (positive) or destabilizing (negative). Each term has also been normalized by the total drive of the respective mode for ease of visualization. The resistive terms sum to a negative contribution quantifying the destabilizing effect of resistive diffusion. Among the resistive terms, the $\mathbf{Q}_\eta \cdot \mathbf{Q}_i$ term is the most negative. All other resistive terms are positive and at least two orders of magnitude smaller. We observe that resistive diffusion cancels most but not all of the ideal stabilizing terms by weakening the effect of field-line bending forces. As a result, the sum of the stabilizing and resistive effects is smaller than the total drive for each mode, resulting in a pos-

itive growth rate.

We define the net stabilization for each mode as the sum of the respective ideal-MHD stabilizing terms and the resistive terms. Its magnitude is compared separately with the parallel current-drive term and the pressure-drive term in Figure 12. It is observed that for each eigenmode, the net stabilization (blue) is larger than either of the two drives in this system. Moreover, the pressure drive is always comparable in magnitude to the parallel current drive. For equilibria from the non-linear computations with viscous heating, the pressure drive is larger than the parallel current drive for some of the eigenmodes (see Figure 13).

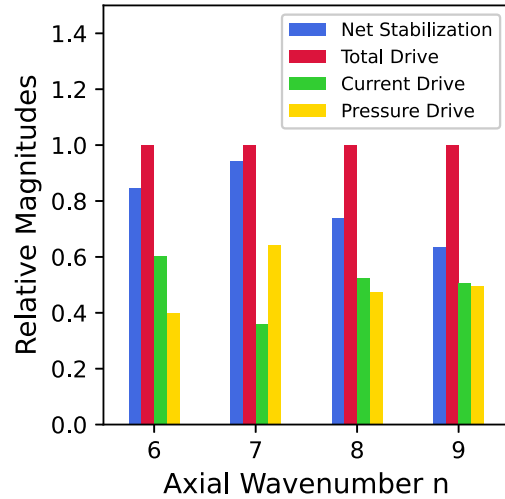


FIG. 12: Kinetic energy integral terms, grouped by the net stabilizing contribution from ideal and resistive terms and compared to the total and individual drives. The analyzed eigenmodes are for the time-averaged profiles from the nonlinear low- β computation without viscous heating.

The above kinetic energy integral analysis for comparing the tearing-mode drives is an analog of the ideal-MHD energy principle for the non-ideal case. In the presence of resistive diffusion, the resulting force operator is not self-adjoint, and a straightforward description of the energy principle is not plausible.⁶⁴ Unlike the ideal-MHD principle,

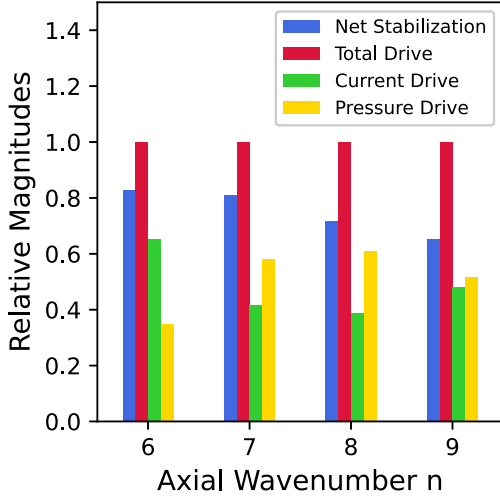


FIG. 13: Kinetic energy integral terms, grouped by the net stabilizing contribution from ideal and resistive terms and compared to the total and individual drives. The analyzed eigenmodes are for the time-averaged profiles from the nonlinear low- β computation with viscous heating.

our kinetic energy integral analysis is not intended to assess the stability of equilibria. The stability of equilibria is described by growth rates of the eigenmodes obtained in the linear computations. Figure 14 shows growth rates of order 10^{-3} obtained for $n=6$ to $n=9$ in our linear calculations with equilibria extracted at different times in the low- β nonlinear saturated state without viscous heating. Here, the profiles are not time-averaged, and the variability over time results from the evolution of the profiles through dynamo activity and transport.

B. Energy Transport

In this section, we describe global energy transport observed in the relaxed state of our nonlinear computations. The spatial profiles of the conductive and convective heat-flux densities are calculated for different times during the saturation phase and averaged over the azimuthal and axial directions

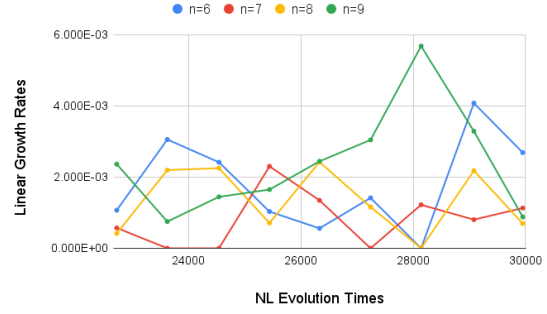


FIG. 14: Linear eigenmode growth rates of $n = 6-9$ obtained from saturated equilibria extracted at different times in the nonlinear evolution.

to obtain radial profiles of outward thermal transport. The outward components of the conductive and convective heat-flux densities are defined as:

$$q_{\parallel r} = \hat{\mathbf{r}} \cdot \mathbf{q}_{\parallel} = -\hat{\mathbf{r}} \cdot \hat{\mathbf{b}} \hat{\mathbf{b}} \cdot (n\chi_{\parallel} \nabla T) \quad (17)$$

$$q_{\perp r} = -\hat{\mathbf{r}} \cdot (n\chi_{\perp} \nabla T) \quad (18)$$

$$q_{conv,r} = \hat{\mathbf{r}} \cdot \left(\frac{\Gamma}{\Gamma-1} nT\mathbf{V} \right) \quad (19)$$

where the subscript 'r' denotes the outward normal direction in cylindrical geometry. Here, $q_{\perp r}$ is considered an isotropic part that has negligible contribution to the parallel direction.

To calculate the net flow of heat across a given radius, the above heat flux densities are integrated over the respective cylindrical surfaces. The resulting quantity is the heat flux denoted by $\langle Q \rangle$:

$$\begin{aligned} \langle Q \rangle &= \int dVol (\nabla \cdot \mathbf{q}) \\ &= \oint r q_r d\theta dz = 4\pi^2 R r \langle q_r \rangle \end{aligned} \quad (20)$$

Q is positive for heat going radially outwards across a given surface. We note that $\langle q_{\parallel r} \rangle$ only results from the correlation of magnetic-field and q_{\parallel} fluctuations. Convective transport can result from the correlation of fluctuations and from average radial flow.

In Figure 15, temporal averages of the inte-

grated parallel and perpendicular thermal conduction and convective heat fluxes are plotted for the low- β saturated state without viscous heating. We observe that the largest contribution to radially outward energy transport in the core comes from the fluctuation-induced $\langle Q_{\parallel} \rangle$. The convective transport is small in the core, and perpendicular thermal conduction is almost negligible. With V_r and B_r approaching zero near the wall and no radiative loss, perpendicular thermal conduction must account for all heat transport near the boundary of our simulations.

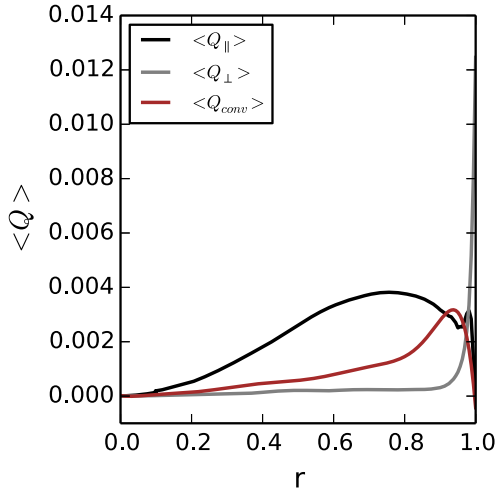


FIG. 15: Profiles of time-averaged fluctuation-induced (parallel), perpendicular, and convective heat flux.

The sum of heat fluxes due to thermal conduction and convection is compared to the enclosed Ohmic heating, as a function of r , to check for energy balances in the final relaxed state. The total outward energy transport is almost equal to the enclosed Ohmic heating across the profile, as shown in Figure 16. The final state is thus self-consistent with respect to energy transport. The excess transport at the extreme edge is considered a minor discrepancy that may arise from an under-resolved boundary layer.

It is useful to decompose the heat flux den-

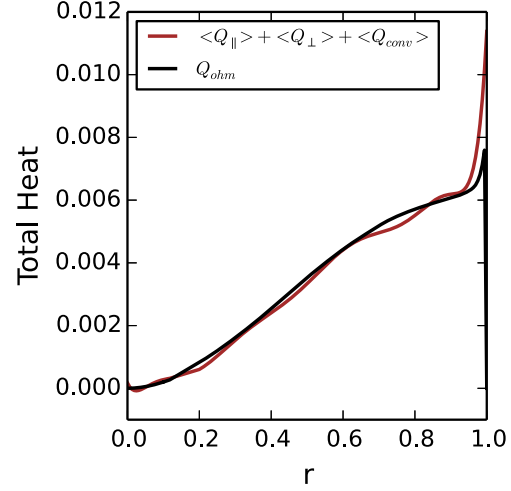


FIG. 16: Profile of total outward heat flux compared with the Ohmic heat enclosed at each radius.

sities analytically by Fourier harmonics to assess which nonlinear perturbations are most responsible for energy transport in the radially outward direction. To achieve this, a mean-field approach is adopted, where each quantity can be split into equilibrium and fluctuating parts:

$$\begin{aligned}
 q_{\parallel r} &= -\hat{\mathbf{r}} \cdot \hat{\mathbf{b}} \hat{\mathbf{b}} \cdot (n \chi_{\parallel} \nabla T) \\
 &= -\frac{\chi_{\parallel}}{B^2} \hat{\mathbf{r}} \cdot (\mathbf{B}_0 + \tilde{\mathbf{B}}) (\mathbf{B}_0 + \tilde{\mathbf{B}}) \cdot (n_0 \nabla T_0 + n_0 \nabla \tilde{T} \\
 &\quad + \tilde{n} \nabla T_0 + \tilde{n} \nabla \tilde{T}) \quad (21)
 \end{aligned}$$

For cylindrical geometry, $\mathbf{B}_0 \cdot \hat{\mathbf{r}} = 0$, and χ_{\parallel} is uniform in our simulations. We expand the above expression and average over the azimuthal and axial directions to obtain radial profiles. Averaging eliminates linear terms, and we obtain:

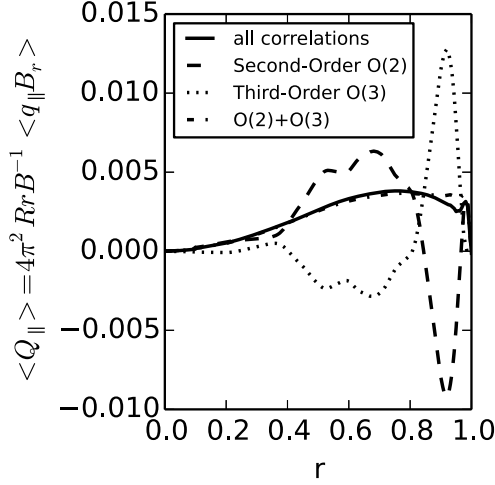


FIG. 17: Time-averaged fluctuation induced conductive heat flux. The 'all' trace refers to contributions from all orders of correlations, O(2) corresponds to only quadratic correlations and O(3) corresponds to only cubic correlations.

$$\begin{aligned} \langle q_{\parallel r} \rangle = & -\frac{\chi_{\parallel}}{B^2} \left[\langle n_0 \tilde{B}_r (\tilde{\mathbf{B}} \cdot \nabla T_0) \rangle + \langle n_0 \tilde{B}_r (\mathbf{B}_0 \cdot \nabla \tilde{T}) \rangle \right. \\ & + \langle n_0 \tilde{B}_r (\tilde{\mathbf{B}} \cdot \nabla \tilde{T}) \rangle + \langle \tilde{n} \tilde{B}_r (\tilde{\mathbf{B}} \cdot \nabla T_0) \rangle \\ & \left. + \langle \tilde{n} \mathbf{B}_0 (\tilde{\mathbf{B}} \cdot \nabla \tilde{T}) \rangle + \langle \tilde{n} \tilde{B}_r (\tilde{\mathbf{B}} \cdot \nabla \tilde{T}) \rangle \right] \end{aligned} \quad (22)$$

where we also use $\mathbf{B}_0 \cdot \nabla T_0 = 0$. The B^2 in the denominator can be expanded with the first two terms of the Taylor expansion so that:

$$\frac{1}{B^2} = \frac{1}{B_0^2} \left(1 - \frac{2\mathbf{B}_0 \cdot \tilde{\mathbf{B}}}{B_0^2} \right) \quad (23)$$

Splitting the terms from Eq. 22 into second-order and third-order correlations and ignoring terms containing $\mathbf{B}_0 \cdot \tilde{\mathbf{B}}$, as they are observed to be very small, we have:

$$\langle q_{\parallel r} \rangle^{(2)} = -\frac{\chi_{\parallel}}{B_0^2} \left[\langle n_0 \tilde{B}_r (\tilde{\mathbf{B}} \cdot \nabla T_0) \rangle + \langle n_0 \tilde{B}_r (\mathbf{B}_0 \cdot \nabla \tilde{T}) \rangle \right] \quad (24)$$

$$\begin{aligned} \langle q_{\parallel r} \rangle^{(3)} = & -\frac{\chi_{\parallel}}{B_0^2} \left[\langle n_0 \tilde{B}_r (\tilde{\mathbf{B}} \cdot \nabla \tilde{T}) \rangle \right. \\ & \left. + \langle \tilde{n} \tilde{B}_r (\tilde{\mathbf{B}} \cdot \nabla T_0) \rangle + \langle \tilde{n} \tilde{B}_r (\mathbf{B}_0 \cdot \nabla \tilde{T}) \rangle \right] \end{aligned} \quad (25)$$

The correlations of parallel heat-flux density fluctuations with magnetic fluctuations at second and third order are plotted in Figure 17. We observe that near $r=0.8$, the second-order radial heat flux goes to zero, and the flow of heat via second-order correlations in the edge is inwards toward the core. Thus, when $\langle q_{\parallel r} \rangle$ is decomposed as shown in Eqs. 24-25, quadratic correlations do not provide a complete description of outward transport observed in the RFP simulation. The third-order correlations sum to a positive value in the edge and are larger than the magnitude of the second-order correlations. The sum of the second and third-order correlations is also shown in the plot and is almost equivalent to the total conductive heat flux from all orders. Thus, we conclude that the fourth and higher-order correlations are small.

The second-order correlations of conductive heat flux, separated by Fourier harmonic from $n=0$ to $n=25$, are shown in Figure 18. Contributions from larger- n components are small and are not included in the plot. As expected, the largest contributors to outward energy transport in the core are the $5 \leq n \leq 13$ components that are associated with tearing fluctuations.

The decomposition of heat flux into terms of different orders of correlation can also be applied to the outward convective transport. The average radial profile of outward convective heat flux density

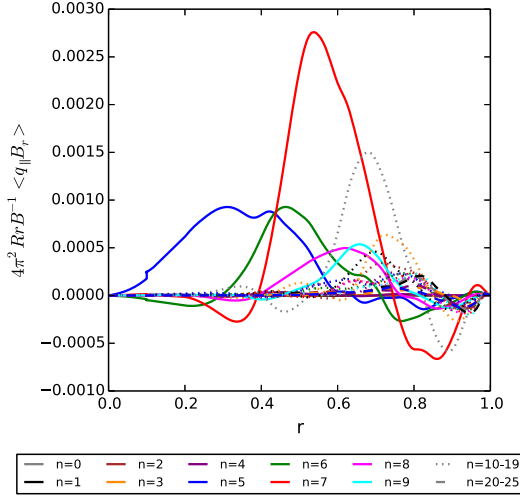


FIG. 18: Quadratic correlations of fluctuation-induced parallel conductive heat flux in the relaxed state of the low- β computation, separated by axial Fourier wavenumber.

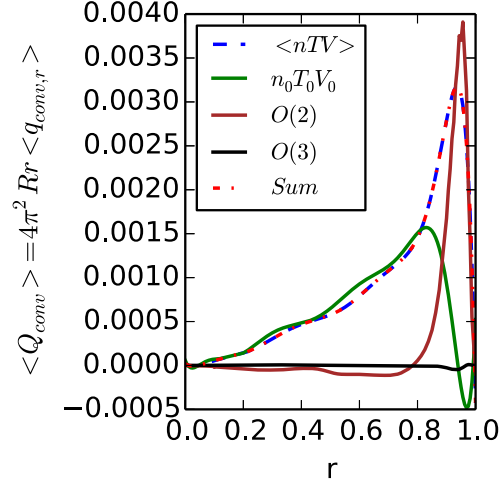


FIG. 19: Convective heat flux as a function of the radial coordinate for the low- β computation. The legend does not show $\Gamma/\Gamma - 1$, but this factor is included in the data.

is given by:

$$\begin{aligned} \langle q_{conv,r} \rangle &= \frac{\Gamma}{\Gamma-1} \langle nTV_r \rangle \\ &= \frac{\Gamma}{\Gamma-1} \langle (n_0 + \tilde{n})(T_0 + \tilde{T})(V_{0r} + \tilde{V}_r) \rangle \end{aligned} \quad (26)$$

The terms that are linear in fluctuating quantities are eliminated by averaging, and we are left with second and third-order correlations:

$$\begin{aligned} \langle Q \rangle_{conv,r}^{(2)} &= C_0 r [n_0 \langle \tilde{T}\tilde{V}_r \rangle + T_0 \langle \tilde{n}\tilde{V}_r \rangle \\ &\quad + \langle \tilde{n}\tilde{T} \rangle V_{0r}] \end{aligned} \quad (27)$$

$$\langle Q \rangle_{conv,r}^{(3)} = C_0 r \langle \tilde{n}\tilde{T}\tilde{V}_r \rangle \quad (28)$$

where $C_0 = \frac{4\pi^2 R\Gamma}{\Gamma-1}$ is a constant.

The convective heat flux crossing a given cylindrical surface is shown in Figure 19. The second-order correlations are small and negative in the core, implying a small amount of inward transport. In

the edge, second-order correlations result in large net outward energy transport. Third-order correlations are an order of magnitude smaller. However, the sum of second and third-order correlations does not explain the total outward convective transport in the core. The zeroth-order term provides the largest contribution, and the sum of the zeroth, second, and third-order terms is nearly equal to the total convective transport.

Because the steady states used to drive the simulations have no pinch flow, the nonzero V_{0r} results from the simulated relaxation with transport. Figure 20 shows that $n = 0$ diffusion is a large part of the particle transport in the simulation. The diffusive flux is negative, implying that it acts as a source, which is balanced by the convective particle transport from $n = 0$ flow and correlations of fluctuations. The sum of the convective and diffusive fluxes is nearly zero over most of the profile, which means that on average, the simulated relaxed state satisfies steady particle transport. The $n_0 V_{0r}$ contribution is a significant component, and the consequence for thermal energy transport is the

$(5/2)n_0T_0V_{0r}$ convective transport. The correction terms for particle diffusion that are included in the temperature evolution equation, Eq. 8 prevent unphysical energy gain or loss in the system from the numerical particle diffusion and do not contribute to heat transport. Not shown are results from a simulation without particle diffusion that is continued from a segment of the low- β simulation. Without the diffusive particle flux, the total convective particle flux sums to zero with fluctuations balancing n_0V_{0r} . The $(5/2)n_0T_0V_{0r}$ convective heat flux in the core is reduced but is still appreciable.

C. Comparison to experiment

Comparing energy transport represented in the computations with experimental results from the Madison Symmetric Torus Experiment provides information on the MHD model's validity for integrated simulation of the system. The radially outward heat flux induced by magnetic fluctuations measured in the edge of MST ($r/a > 0.75$) is shown in Figure 21. It is described as the second-order correlation of the fluctuating heat-flux density parallel

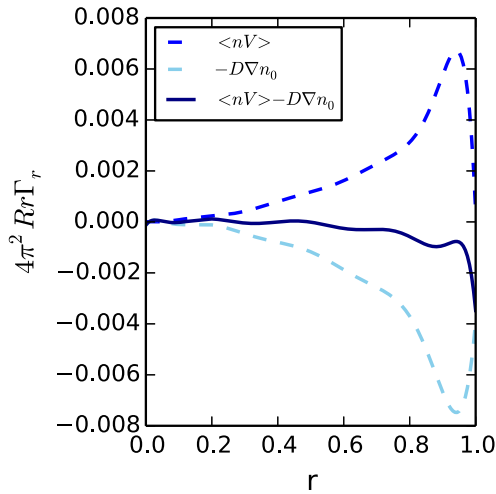


FIG. 20: Particle flux as a function of the radial coordinate for the low- β computation.

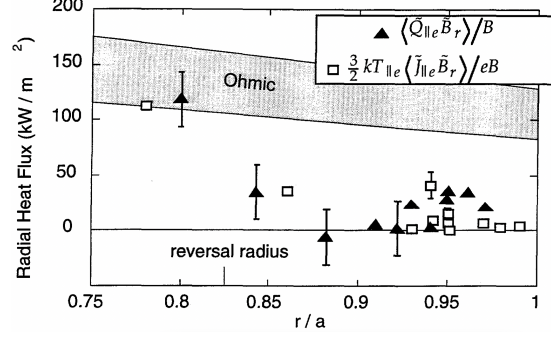


FIG. 21: Experimental measurements of fluctuation induced heat fluxes and particle fluxes in the edge of MST-RFP experiment. Reproduced with permission from Fiksel, *et al.*, Plasma Phys. Control. Fusion **38**, A213 (1996).⁶⁵ Copyright 1996 IOP Publishing Ltd.

to the equilibrium magnetic field and the fluctuating radial component of magnetic field. This quadratic correlation is

$$Q_r = \frac{\langle \tilde{q}_{\parallel} \tilde{B}_r \rangle}{B_0} = \frac{\langle \tilde{\mathbf{q}} \cdot \mathbf{B}_0 \tilde{B}_r \rangle}{B_0^2} \quad (29)$$

where \tilde{q}_{\parallel} is the total heat flux density parallel to the equilibrium magnetic field, \tilde{B}_r is the fluctuating magnetic field in the radial direction, and \mathbf{B}_0 is the equilibrium magnetic field. Both fluctuating quantities are measured locally with probes. Here, the symbol $\langle \rangle$ represents an ensemble average of many time records in the experiment, where instantaneous surface averaging is not possible. The correlations just inside the reversal surface yield a heat flux that accounts for the energy transport expected from Ohmic input. This flux is analogous to the sum of the last terms on the right sides of Eqs. 24 and 25. The third-order term in our analysis would be considered part of the quadratic correlation for the experiment, because the experimentally measured $\tilde{\mathbf{q}} \cdot \mathbf{B}_0$ is not decomposed. Also, Fiksel, *et al.* state that the third-order correlation associated with magnetic compression $\langle \tilde{q}_{\parallel} \tilde{B}_{\parallel} \tilde{B}_r \rangle / B_0^2$ is measured to be small,¹⁹ as we have found in the MHD simulations.

Fiksel, *et al.* also found the fluctuation-induced heat flux near the reversal surface to be from con-

vection. An independent measurement determined the fluctuation-induced electron particle flux $\Gamma_r = \langle \tilde{\Gamma}_{e\parallel} \tilde{B}_r \rangle / B$ from fluctuations in the parallel electron particle flux, $\tilde{\Gamma}_{e\parallel}$. The electron energy distribution was measured to be anisotropic in the edge of MST, and as shown in Figure 21, the convection of energy in random parallel motions $\tilde{Q}_{conv,r} = 3/2 k_B T_{\parallel e} \Gamma_r$ was found to match the fluctuation-induced heat flux in the MST edge plasma.^[19] The heat flux inside the reversal surface was also found to follow Rechester-Rosenbluth (RR) collisionless transport along stochastic magnetic field,^[18] provided that the electron thermal velocity is replaced by the ion thermal velocity.^[65]

The theoretical developments in Ref. 66 investigate kinetic shielding and drag effects from quasineutrality and induced magnetic fluctuations when the electron distribution has clumps of electrons streaming along perturbed magnetic field-lines. Over the edge region of MST, the dominant magnetic fluctuations are from the global tearing modes, which are resonant in the core. The theory predicts that the non-resonant nature of the fluctuations reduces the turbulent electron-electron diffusivity, which leads to the "ambipolar" property of ion thermal speed limiting the edge electron energy transport. In the core, where the dominant modes are resonant, the turbulent energy transport does not follow an ambipolar constraint.

More recent analysis of fluctuation-induced thermal transport in MST was performed by Biewer *et al.* using MST's Thomson scattering diagnostic.^[20] The total thermal conductive and convective heat fluxes were estimated from a local power balance equation by taking into account heating sources, as well as all possible sinks such as particle collisions, radiative losses, and ambipolar particle transport. The measurements found convective heat flux to account for less than 10% of the total heat flux in the core, as shown in Figure 22. In addition, the core transport is consistent with the RR magnetic diffusivity using the electron thermal speed, where the magnetic diffusivity is inferred with scaled magnetic fluctuations from DEBS MHD simulations. This behavior agrees with the theoretical expectations for resonant magnetic fluctuation-induced heat flux.^[66]

When comparing energy transport results from

our simulation and from MST, we note the qualitative agreement of heat flux from correlations of magnetic and parallel heat-flux-density fluctuations being the largest contribution in the core. The simulations use fixed χ_{\parallel} and χ_{\perp} values at a ratio that is much smaller than in MST's core, but the modeled transport results from the large anisotropy along temporally evolving 3D magnetic field. Using a greater χ_{\parallel} -value may further increase the resulting ratio of conductive and convective transport to approach the experimental findings in Figure 22. However, the MHD modeling cannot reproduce the kinetic effects that describe streaming in the electron distribution and distinguish resonant and non-resonant responses. Also, while fluctuation-induced convective transport is important in the edge of the simulations, reminiscent of Ref. 19, it is from an MHD \tilde{V}_r , and not from a $\tilde{\Gamma}_{e\parallel}$, as found from probe measurements. In addition, important particle-transport processes, including interaction with neutrals near the wall, are not represented and likely affect convective heat transport in the edge.

Despite the very simplified modeling of transport, it is worth emphasizing the comprehensive nature of our simulations. They determine the 3D evolution of all fields with current-drive, heating, and the simplified energy and particle transport processes. The evolution also maintains approximate MHD force-balance of the large-scale fields. The computations allow us to examine nonlinear interactions as they evolve and self-consistently settle into a relaxed RFP state that is close to marginal stability. The qualitative agreement of the simulations with conventional multi-helicity RFP experiments can be attributed to the importance of the tearing fluctuations, which the MHD simulations model well.

V. SUMMARY AND CONCLUSIONS

The study presented in this article applies nonlinear MHD simulation to model tearing dynamics, magnetic relaxation, and energy transport in inductively driven multi-helicity RFPs. Our computations with the NIMROD code use unstable symmetric steady-state solutions of the dynamical equa-

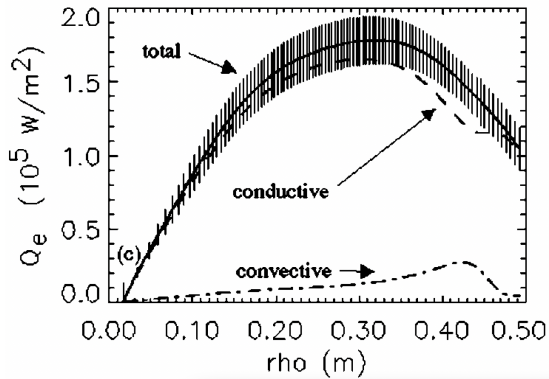


FIG. 22: Fluctuation induced heat fluxes as observed in the sawtooth crash phase of the MST-RFP experiment. Reproduced with permission from Biewer, *et al.*, Phys. Rev. Lett. **91**, 045004 (2003).^[20] Copyright 2003 The American Physical Society.

tions to drive the relaxation dynamics while avoiding large-scale pinching. The simulations evolve to experimentally relevant regimes, as found previously with similar MHD models without density evolution^[38] and with density evolution at smaller Lundquist number.^[46] Our analysis of the relaxed states includes: 1) confirming power flow through the dynamo effect to sustain relaxation,^[8] 2) comparing pressure and curvature drives of tearing in the relaxed states, and 3) identifying the correlations that lead to energy transport. The dynamo effect and energy transport are diagnosed directly from the 3D simulation results. The pressure drive for tearing is determined through kinetic-energy considerations for linear eigenmodes of the relaxed profiles.

We find that the linearly unstable low-wavenumber modes of profiles extracted from our nonlinear computations have tearing parity. That is consistent with previous linear computations of pressure-driven MHD modes for prescribed, mathematically simple, Δ' -stable RFP profiles.^[30,31] Moreover, we quantify the pressure-gradient drive by analyzing all terms that contribute to the kinetic energy integral in the linear computations. This analysis finds the pressure-gradient drive to be comparable to the parallel-current drive for these tearing-parity modes and that neither drive alone exceeds

the combination of ideal-MHD stabilizing and resistive diffusion terms. Thus, we infer that pressure is significant in driving the dynamo modes in the nonlinear RFP computations that sustain a pressure gradient. Our dynamo-effect analysis shows the same behavior as in simulations without pressure evolution, so the significance of the pressure drive does not modify well-established insights on RFP tearing with respect to field reversal.

The computational diagnostics of heat transport in the simulations is qualitatively consistent with a previous analysis of MST experiments^[20] in that transport induced by magnetic perturbations from tearing is largest in the core. The fluctuation-induced core transport in the simulations is conductive, Eq. [22](#). Deconstruction of the simulated conductive heat flux into correlations of temperature, density, and magnetic fluctuations shows that second-order correlations alone do not explain parallel thermal transport in our nonlinear computations. Third-order correlations are important in forming the outward transport process. The experimental study concluded that core MST transport is also conductive by considering collisionless RR stochastic-field analysis. That random-walk analysis uses test-particle streaming to yield thermal conduction on the scale of the experiment. It differs from the locally anisotropic conduction along 3D fields in the MHD simulations, but the two lead to qualitatively similar transport.

To achieve more representative integrated simulations will require two-fluid modeling to reproduce drift effects, as in previous RFP computations^[48] but with a pressure profile. Better modeling of the edge is also important, as the post-relaxation pressure profile (Figure [7](#)) has its gradient unrealistically close to the wall. Temperature-dependent thermal diffusivities may help in this regard, but the $\chi_{\parallel}/\chi_{\perp}$ -ratio in our simulations is already more representative of edge conditions than core conditions. Interaction with neutral particles is important near the wall in the experiment and can be incorporated with a dynamic neutral model,^[67] which has recently been added to NIMROD.^[68] In principle, the kinetic physics of fluctuation-induced energy transport can also be included through integrated MHD/drift-kinetic modeling,^[69] but including two velocity-space dimensions will lead to signif-

icantly larger computational costs than the simulations presented here.

ACKNOWLEDGMENTS

The authors wish to acknowledge Prof. John Sarff for many helpful discussions about the MST-RFP experiment. We would also like to thank Prof. Chris Hegna and Prof. Paul Terry for their insights on RFP Theory. This research is supported by the U.S. Department of Energy (DOE) Grant No. DE-FG02-85ER53212. This research used resources of the National Energy Research Scientific Computing Center (NERSC), a U.S. Department of Energy Office of Science User Facility located at Lawrence Berkeley National Laboratory, operated under Contract No. DE-AC02-05CH11231 using NERSC award ERCAP0020418.

- ¹J. B. Taylor. Relaxation of Toroidal Plasma and Generation of Reverse Magnetic Fields. *Physical Review Letters*, 33(19):1139–1141, November 1974. Publisher: American Physical Society. [1](#)
- ²S. C. Prager. Transport and fluctuations in reversed field pinches. *Plasma Physics and Controlled Fusion*, 32(11):903–916, November 1990. Publisher: IOP Publishing. [1](#)
- ³H. A. B. Bodin and A. A. Newton. Reversed-field-pinch research. *Nuclear Fusion*, 20(10):1255–1324, October 1980. Publisher: IOP Publishing. [1](#)
- ⁴L. Marrelli, P. Martin, M. E. Puiatti, J. S. Sarff, B. E. Chapman, J. R. Drake, D. F. Escande, and S. Masamune. The reversed field pinch. *Nuclear Fusion*, 61(2):023001, January 2021. Publisher: IOP Publishing. [1](#)
- ⁵A. Y. Aydemir and D. C. Barnes. Sustained Self-Reversal in the Reversed-Field Pinch. *Physical Review Letters*, 52(11):930–933, March 1984. Publisher: American Physical Society. [1](#)
- ⁶D. D. Schnack, E. J. Caramana, and R. A. Nebel. Three-dimensional magnetohydrodynamic studies of the reversed-field pinch. *The Physics of Fluids*, 28(1):321–333, January 1985. Publisher: American Institute of Physics. [3](#)
- ⁷J. A. Holmes, B. A. Carreras, P. H. Diamond, and V. E. Lynch. Nonlinear dynamics of tearing modes in the reversed field pinch. *The Physics of Fluids*, 31(5):1166–1179, May 1988. Publisher: American Institute of Physics.
- ⁸Y. L. Ho. Numerical simulation of fluctuation suppression via DC helicity injection in a reversed field pinch. *Nuclear Fusion*, 31(2):341–350, February 1991. Publisher: IOP Publishing. [3](#) [20](#)
- ⁹S. Cappello and D. Biskamp. Reconnection processes and scaling laws in reversed field pinch magnetohydrodynamics. *Nuclear Fusion*, 36(5):571–581, May 1996. Publisher: IOP Publishing. [2](#) [4](#)
- ¹⁰K. Kusano and T. Sato. Non-linear coupling effects on the relaxation process in the reversed field pinch. *Nuclear Fusion*, 27(5):821–832, May 1987. Publisher: IOP Publishing.
- ¹¹J. R. King, C. R. Sovinec, and V. V. Mirnov. First-order finite-Larmor-radius fluid modeling of tearing and relaxation in a plasma pinch. *Physics of Plasmas*, 19(5):055905, May 2012. [3](#) [8](#)
- ¹²J. P. Sauppe and C. R. Sovinec. Extended MHD modeling of tearing-driven magnetic relaxation. *Physics of Plasmas*, 24(5):056107, May 2017. [1](#) [3](#) [8](#)
- ¹³J. S. Sarff, S. Assadi, A. F. Almagri, M. Cekic, D. J. Den Hartog, G. Fiksel, S. A. Hokin, H. Ji, S. C. Prager, W. Shen, K. L. Sidikman, and M. R. Stoneking. Nonlinear coupling of tearing fluctuations in the Madison Symmetric Torus*. *Physics of Fluids B: Plasma Physics*, 5(7):2540–2545, July 1993. Publisher: American Institute of Physics. [1](#)
- ¹⁴H. Ji, S. C. Prager, and J. S. Sarff. Conservation of Magnetic Helicity during Plasma Relaxation. *Physical Review Letters*, 74(15):2945–2948, April 1995. Publisher: American Physical Society.
- ¹⁵D. J. Den Hartog, J. T. Chapman, D. Craig, G. Fiksel, P. W. Fontana, S. C. Prager, and J. S. Sarff. Measurement of core velocity fluctuations and the dynamo in a reversed-field pinch. *Physics of Plasmas*, 6(5):1813–1821, May 1999. Publisher: American Institute of Physics.
- ¹⁶W. X. Ding, D. L. Brower, D. Craig, B. H. Deng, G. Fiksel, V. Mirnov, S. C. Prager, J. S. Sarff, and V. Svidzinski. Measurement of the Hall Dynamo Effect during Magnetic Reconnection in a High-Temperature Plasma. *Physical Review Letters*, 93(4):045002, July 2004. [8](#)
- ¹⁷A. Kuritsyn, G. Fiksel, A. F. Almagri, D. L. Brower, W. X. Ding, M. C. Miller, V. V. Mirnov, S. C. Prager, and J. S. Sarff. Measurements of the momentum and current transport from tearing instability in the Madison Symmetric Torus reversed-field pinch. *Physics of Plasmas*, 16(5):055903, May 2009. Publisher: American Institute of Physics. [1](#)
- ¹⁸A. B. Rechester and M. N. Rosenbluth. Electron Heat Transport in a Tokamak with Destroyed Magnetic Surfaces. *Physical Review Letters*, 40(1):38–41, January 1978. Publisher: American Physical Society. [1](#) [19](#)
- ¹⁹G. Fiksel, S. C. Prager, W. Shen, and M. R. Stoneking. Measurement of magnetic fluctuation induced energy transport. *Physical Review Letters*, 72(7):1028–1031, February 1994. [18](#) [19](#)
- ²⁰T. M. Biewer, C. B. Forest, J. K. Anderson, G. Fiksel, B. Hudson, S. C. Prager, J. S. Sarff, J. C. Wright, D. L. Brower, W. X. Ding, and S. D. Terry. Electron Heat Transport Measured in a Stochastic Magnetic Field. *Physical Review Letters*, 91(4):045004, July 2003. [1](#) [19](#) [20](#)
- ²¹J. S. Sarff, A. F. Almagri, J. K. Anderson, M. Borchardt, D. Carmody, K. Caspary, B. E. Chapman, D. J. Den Hartog, J. Duff, S. Eilerman, A. Falkowski, C. B. Forest, J. A. Goetz, D. J. Holly, J.-H. Kim, J. King, J. Ko, J. Koliner, S. Kumar, J. D. Lee, D. Liu, R. Magee, K. J. McCollam, M. McGarry, V. V. Mirnov, M. D. Nornberg, P. D. Nonn, S. P. Oliva, E. Parke, J. A. Reusch, J. P. Sauppe, A. Seltzman, C. R. Sovinec, H. Stephens, D. Stone, D. Theucks, M. Thomas, J. Triana, P. W. Terry, J. Waksman, W. F. Bergerson, D. L. Brower, W. X. Ding, L. Lin,

- D.R. Demers, P. Fimognari, J. Titus, F. Auremma, S. Cappello, P. Franz, P. Innocente, R. Lorenzini, E. Martinez, B. Momo, P. Piovesan, M. Puiatti, M. Spolaore, D. Terranova, P. Zanca, V. Belykh, V.I. Davydenko, P. Deichuli, A.A. Ivanov, S. Polosatkin, N.V. Stupishin, D. Spong, D. Craig, R.W. Harvey, M. Cianciosa, and J.D. Hanson. Overview of results from the MST reversed field pinch experiment. *Nuclear Fusion*, 53(10):104017, October 2013. [2](#)
- ²²D. Bonfiglio, M. Veranda, S. Cappello, D. F. Escande, and L. Chacón. Experimental-like Helical Self-Organization in Reversed-Field Pinch Modeling. *Physical Review Letters*, 111(8):085002, August 2013. [2](#)
- ²³D. C. Robinson. High- diffuse pinch configurations. *Plasma Physics*, 13(6):439–462, June 1971. Publisher: IOP Publishing. [2](#)
- ²⁴Harold P. Furth, John Killeen, and Marshall N. Rosenbluth. Finite-Resistivity Instabilities of a Sheet Pinch. *The Physics of Fluids*, 6(4):459–484, April 1963. Publisher: American Institute of Physics. [2](#)
- ²⁵John L. Johnson, John M. Greene, and Bruno Coppi. Effect of Resistivity on Hydromagnetic Instabilities in Multipolar Systems. *Physics of Fluids*, 6(8):1169, 1963. [2](#)
- ²⁶Bruno Coppi, John M. Greene, and John L. Johnson. Resistive instabilities in a diffuse linear pinch. *Nuclear Fusion*, 6(2):101–117, June 1966. [2](#)
- ²⁷John M. Finn and Wallace M. Manheimer. Resistive interchange modes in reversed-field pinches. *The Physics of Fluids*, 25(4):697–701, April 1982. Publisher: American Institute of Physics. [2](#)
- ²⁸D. Merlin, S. Ortolani, R. Paccagnella, and M. Scapin. Linear resistive magnetohydrodynamic stability analysis of reversed field pinch configurations at finite beta. *Nuclear Fusion*, 29(7):1153–1160, July 1989. Publisher: IOP Publishing. [2](#)
- ²⁹D. H. Liu. Effects of current and pressure profiles on resistive MHD modes in reversed field pinches. *Nuclear Fusion*, 37(8):1083–1093, August 1997. Publisher: IOP Publishing. [2](#)
- ³⁰F. Ebrahimi, S. C. Prager, and C. R. Sovinec. Resistive-ideal transition of pressure-driven instabilities in current-carrying plasmas beyond the Suydam criterion. *Physics of Plasmas*, 9(6):2470–2473, June 2002. [2](#) [20](#)
- ³¹R. Paccagnella. Pressure driven tearing and interchange modes in the reversed field pinch. *Physics of Plasmas*, 20(1):012119, January 2013. [2](#) [20](#)
- ³²Hinrich Lütjens, Jean-François Luciani, and Xavier Garbet. Curvature effects on the dynamics of tearing modes in tokamaks. *Physics of Plasmas*, 8(10):4267–4270, October 2001. [2](#)
- ³³Richard Fitzpatrick. Helical temperature perturbations associated with tearing modes in tokamak plasmas. *Physics of Plasmas*, 2(3):825–838, March 1995. Publisher: American Institute of Physics. [2](#)
- ³⁴A. Bruno, J. P. Freidberg, and R. J. Hastie. Resistive magnetohydrodynamic transport model for a reversed field pinch. I. The model. *Physics of Plasmas*, 10(6):2330–2339, June 2003. [2](#)
- ³⁵Ahmed Akram Mirza, Jan Scheffel, and Thomas Johnson. Effect of thermal conduction on pressure-driven modes in the reversed-field pinch. *Nuclear Fusion*, 52(12):123012, December 2012. [2](#)
- ³⁶D. D. Schnack, J. Killeen, and R. A. Gerwin. The non-linear evolution of resistive interchange modes in a reversed-field pinch. *Nuclear Fusion*, 21(11):1447–1456, November 1981. Publisher: IOP Publishing. [3](#)
- ³⁷Carl Sovinec. Magnetohydrodynamic simulations of non-inductive helicity injection in the reversed-field pinch and tokamak. *University of Wisconsin-Madison*, 1995. [3](#)
- ³⁸J. Scheffel and D. D. Schnack. Numerical studies of confinement scaling in the conventional reversed field pinch. *Nuclear Fusion*, 40(11):1885–1896, November 2000. Publisher: IOP Publishing. [3](#) [20](#)
- ³⁹J. Scheffel and J.-E. Dahlin. Confinement scaling in the advanced reversed-field pinch. *Plasma Physics and Controlled Fusion*, 48(11):L97–L104, October 2006. Publisher: IOP Publishing. [3](#)
- ⁴⁰J.-E. Dahlin and J. Scheffel. Numerical studies of confinement scalings for the dynamo-free reversed-field pinch. *Nuclear Fusion*, 47(1):9–16, December 2006. Publisher: IOP Publishing. [3](#)
- ⁴¹J. S. Sarff, S. A. Hokin, H. Ji, S. C. Prager, and C. R. Sovinec. Fluctuation and transport reduction in a reversed field pinch by inductive poloidal current drive. *Physical Review Letters*, 72(23):3670–3673, June 1994. Publisher: American Physical Society. [3](#)
- ⁴²J. S. Sarff, N. E. Lanier, S. C. Prager, and M. R. Stoneking. Increased Confinement and β by Inductive Poloidal Current Drive in the Reversed Field Pinch. *Physical Review Letters*, 78(1):62–65, January 1997. Publisher: American Physical Society.
- ⁴³C. R. Sovinec and S. C. Prager. Magnetohydrodynamic effects of current profile control in reversed field pinches. *Nuclear Fusion*, 39(6):777–790, June 1999. Publisher: IOP Publishing.
- ⁴⁴J. M. Reynolds, C. R. Sovinec, and S. C. Prager. Nonlinear magnetohydrodynamics of pulsed parallel current drive in reversed-field pinches. *Physics of Plasmas*, 15(6):062512, June 2008. Publisher: American Institute of Physics. [3](#)
- ⁴⁵M. Onofri, F. Malara, and P. Veltri. Effects of Anisotropic Thermal Conductivity in Magnetohydrodynamics Simulations of a Reversed-Field Pinch. *Physical Review Letters*, 105(21):215006, November 2010. Publisher: American Physical Society. [3](#)
- ⁴⁶M. Onofri, F. Malara, and P. Veltri. Role of anisotropic thermal conductivity in the reversed-field pinch dynamics. *Physics of Plasmas*, 18(5):052502, May 2011. Publisher: American Institute of Physics. [3](#) [20](#)
- ⁴⁷V. V. Mirnov, C. C. Hegna, and S. C. Prager. Two-fluid tearing instability in force-free magnetic configuration. *Physics of Plasmas*, 11(9):4468–4482, September 2004. Publisher: American Institute of Physics. [3](#)
- ⁴⁸J. R. King, C. R. Sovinec, and V. V. Mirnov. First-order finite-Larmor-radius effects on magnetic tearing in pinch configurations. *Physics of Plasmas*, 18(4):042303, April 2011. [3](#) [8](#) [20](#)
- ⁴⁹We avoid the term “resistive g-mode,” which is used to refer to resistive interchange or to any pressure-driven resistive mode in the literature. [3](#)
- ⁵⁰C.R. Sovinec, A.H. Glasser, T.A. Gianakon, D.C. Barnes, R.A.

- Nebel, S.E. Kruger, D.D. Schnack, S.J. Plimpton, A. Tarditi, and M.S. Chu. Nonlinear magnetohydrodynamics simulation using high-order finite elements. *Journal of Computational Physics*, 195(1):355–386, March 2004. [3](#) [6](#)
- ⁵¹E.C. Howell and C.R. Sovinec. Solving the Grad–Shafranov equation with spectral elements. *Computer Physics Communications*, 185(5):1415–1421, May 2014. [3](#)
- ⁵²Harold Grad and Hanan Rubin. Hydromagnetic equilibria and force-free fields. *Journal of Nuclear Energy (1954)*, 7(3):284–285, 1958. [4](#)
- ⁵³V D Shafranov. ON MAGNETOHYDRODYNAMICAL EQUILIBRIUM CONFIGURATIONS. *Soviet Physics JETP*, 6(3):545–554, 1958. [4](#)
- ⁵⁴K. J. Bunkers and C. R. Sovinec. The influence of boundary and edge-plasma modeling in computations of axisymmetric vertical displacement. *Physics of Plasmas*, 27(11):112505, November 2020. [6](#)
- ⁵⁵A. Y. Aydemir, D. C. Barnes, E. J. Caramana, A. A. Mirin, R. A. Nebel, D. D. Schnack, and A. G. Sgro. Compressibility as a feature of field reversal maintenance in the reversed-field pinch. *Physics of Fluids*, 28(3):898, 1985. [8](#)
- ⁵⁶M. Onofri, F. Malara, and P. Veltri. Effects of compressibility and heating in magnetohydrodynamics simulations of a reversed field pinch. *Physics of Plasmas*, 16(5):052508, May 2009. [8](#)
- ⁵⁷D.J. Den Hartog, J.-W. Ahn, A.F. Almagri, J.K. Anderson, A.D. Beklemishev, A.P. Blair, F. Bonomo, M.T. Borchardt, D.L. Brower, D.R. Burke, M. Cengher, B.E. Chapman, S. Choi, D.J. Clayton, W.A. Cox, S.K. Combs, D. Craig, H.D. Cummings, V.I. Davydenko, D.R. Demers, B.H. Deng, W.X. Ding, F. Ebrahimi, D.A. Ennis, G. Fiksel, C. Foust, C.B. Forest, P. Franz, L. Frassinetti, S. Gangadhara, J.A. Goetz, R.W. Harvey, D.J. Holly, B.F. Hudson, A.A. Ivanov, M.C. Kaufman, A.V. Kuritsyn, A.A. Lizunov, T.W. Lovell, R.M. Magee, L. Marrelli, P. Martin, K.J. McCollam, M.C. Miller, V.V. Mirnov, P.D. Nonn, R. O’Connell, S.P. Oliva, P. Piovesan, S.C. Prager, I. Predebon, J.A. Reusch, J.S. Sarff, V.A. Svidzinski, T.D. Tharp, M.A. Thomas, Yu.A. Tsidulko, M.D. Wyman, and T. Yates. Recent improvements in confinement and beta in the MST reversed-field pinch. *Nuclear Fusion*, 47(9):L17–L20, September 2007. [8](#)
- ⁵⁸B.E. Chapman, J.W. Ahn, A.F. Almagri, J.K. Anderson, F. Bonomo, D.L. Brower, D.R. Burke, K. Caspary, D.J. Clayton, S.K. Combs, W.A. Cox, D. Craig, B.H. Deng, D.J. Den Hartog, W.X. Ding, F. Ebrahimi, D.A. Ennis, G. Fiksel, C.B. Forest, C.R. Foust, P. Franz, S. Gangadhara, J.A. Goetz, M.C. Kaufman, J.G. Kulpin, A. Kuritsyn, R.M. Magee, M.C. Miller, V.V. Mirnov, P.D. Nonn, R. O’Connell, S.P. Oliva, S.C. Prager, J.A. Reusch, J.S. Sarff, H.D. Stephens, M.D. Wyman, and T. Yates. Improved-confinement plasmas at high temperature and high beta in the MST RFP. *Nuclear Fusion*, 49(10):104020, October 2009. [8](#)
- ⁵⁹Y. L. Ho and G. G. Craddock. Nonlinear dynamics of field maintenance and quasiperiodic relaxation in reversed-field pinches. *Physics of Fluids B: Plasma Physics*, 3(3):721–734, March 1991. [8](#)
- ⁶⁰W. X. Ding, D. L. Brower, B. H. Deng, A. F. Almagri, D. Craig, G. Fiksel, V. Mirnov, S. C. Prager, J. S. Sarff, and V. Svidzinski. The Hall dynamo effect and nonlinear mode coupling during sawtooth magnetic reconnection. *Physics of Plasmas*, 13(11):112306, November 2006. [8](#)
- ⁶¹V. V. Mirnov, C. C. Hegna, and S. C. Prager. A hall dynamo effect driven by two-fluid tearing instability. *Plasma Physics Reports*, 29(7):566–570, July 2003.
- ⁶²J. P. Sauppe and C. R. Sovinec. Two-fluid and finite Larmor radius effects on helicity evolution in a plasma pinch. *Physics of Plasmas*, 23(3):032303, March 2016. [8](#)
- ⁶³J. P. Freidberg. *Ideal magnetohydrodynamics*. January 1987. Publisher: Plenum Press, New York, NY. [12](#)
- ⁶⁴A. Pletzer. Energy principles for linear dissipative systems with application to resistive MHD stability. *Physics of Plasmas*, 4(9):3141–3151, September 1997. [13](#)
- ⁶⁵G Fiksel, Roger D Bengtson, M Cekic, D Den Hartog, S C Prager, P Pribyl, J Sarff, C Sovinec, MR Stoneking, RJ Taylor, P W Terry, G R Tynan, and A J Wootton. Measurement of magnetic fluctuation-induced heat transport in tokamaks and RFP. *Plasma Physics and Controlled Fusion*, 38(12A):A213–A225, December 1996. [18](#) [19](#)
- ⁶⁶P. W. Terry, G. Fiksel, H. Ji, A. F. Almagri, M. Cekic, D. J. Den Hartog, P. H. Diamond, S. C. Prager, J. S. Sarff, W. Shen, M. Stoneking, and A. S. Ware. Ambipolar magnetic fluctuation-induced heat transport in toroidal devices. *Physics of Plasmas*, 3(5):1999–2005, May 1996. [19](#)
- ⁶⁷E. T. Meier and U. Shumlak. A general nonlinear fluid model for reacting plasma-neutral mixtures. *Physics of Plasmas*, 19(7):072508, 2012. [20](#)
- ⁶⁸Sina Taheri, Jacob R. King, and Uri Shumlak. Time-discretization of a plasma-neutral mhd model with a semi-implicit leapfrog algorithm. *Computer Physics Communications*, 274:108288, 2022. [20](#)
- ⁶⁹E. D. Held, S. E. Kruger, J.-Y. Ji, E. A. Belli, and B. C. Lyons. Verification of continuum drift kinetic equation solvers in nimrod. *Physics of Plasmas*, 22(3):032511, 2015. [20](#)